

## Mechanical versus kinematical shortening reconstructions of the Zagros High Folded Zone (Kurdistan region of Iraq)

Marcel Frehner,<sup>1,2</sup> Daniel Reif,<sup>1</sup> and Bernhard Grasemann<sup>1</sup>

Received 25 August 2011; revised 7 March 2012; accepted 20 March 2012; published 5 May 2012.

[1] This paper compares kinematical and mechanical techniques for the palinspastic reconstruction of folded cross sections in collision orogens. The studied area and the reconstructed NE–SW trending, 55.5 km long cross section is located in the High Folded Zone of the Zagros fold-and-thrust belt in the Kurdistan region of Iraq. The present-day geometry of the cross section has been constructed from field as well as remote sensing data. In a first step, the structures and the stratigraphy are simplified and summarized in eight units trying to identify the main geometric and mechanical parameters. In a second step, the shortening is kinematically estimated using the dip domain method to 11%–15%. Then the same cross section is used in a numerical finite element model to perform dynamical unfolding simulations taking various rheological parameters into account. The main factor allowing for an efficient dynamic unfolding is the presence of interfacial slip conditions between the mechanically strong units. Other factors, such as Newtonian versus power law viscous rheology or the presence of a basement, affect the numerical simulations much less strongly. If interfacial slip is accounted for, fold amplitudes are reduced efficiently during the dynamical unfolding simulations, while welded layer interfaces lead to unrealistic shortening estimates. It is suggested that interfacial slip and decoupling of the deformation along detachment horizons is an important mechanical parameter that controlled the folding processes in the Zagros High Folded Zone.

**Citation:** Frehner, M., D. Reif, and B. Grasemann (2012), Mechanical versus kinematical shortening reconstructions of the Zagros High Folded Zone (Kurdistan region of Iraq), *Tectonics*, 31, TC3002, doi:10.1029/2011TC003010.

### 1. Introduction

[2] The retrodeformation of geological cross sections is a key tool to unravel the geological deformation history in a certain area. When the deformation is dominated by folding, the shortening necessary to produce the observed fold geometries can be estimated from such unfolding calculations. Commonly, the shortening estimates are done based on kinematical reconstructions of balanced cross sections. Kinematical methods only have limited capabilities to account for the different mechanical behaviors of the individual folded units. However, the mechanical behavior and the rheological material parameters can strongly influence the folding process, and purely kinematical shortening estimates may be inaccurate. Understanding the dominating factors that influence the estimated shortening values is therefore fundamental for understanding the evolution of fold-dominated belts in collision orogens.

[3] One way of including the mechanical behavior of the folded layers has been suggested by *Schmalholz* [2008]

and can be termed dynamical unfolding [after *Lechmann et al.*, 2010]. It has been suggested to use the present-day fold geometry as the initial condition of a numerical finite element model for folding, but applying horizontal extensional boundary conditions to dynamically unfold the cross section. This corresponds to a reverse time simulation where the folding process is reversed. It has been shown that this method successfully unfolds two-dimensional synthetic buckle folds in the case of linear (Newtonian) or power law viscous rheology [*Lechmann et al.*, 2010], as well as three-dimensional folds in the case of Newtonian rheology [*Schmalholz*, 2008]. The kinematical unfolding (i.e., constant arc length) of synthetic folds with a known amount of shortening has revealed that the kinematical method underestimates the amount of shortening necessary for a certain fold geometry [*Ghassemi et al.*, 2010; *Lechmann et al.*, 2010]. This mismatch is due to the layer-parallel shortening (and layer thickening) prior to folding, which is not accounted for in kinematical constant arc length methods.

[4] There is a large number of numerical studies investigating the evolution of geological folds [e.g., *Dieterich*, 1969; *Shimamoto and Hara*, 1976; *Lan and Hudleston*, 1991; *Mancktelow*, 1999; *Schmalholz et al.*, 2001; *Schmid et al.*, 2004; *Frehner and Schmalholz*, 2006; *Frehner*, 2011], but most of them consider a forward directed time evolution. Only very few studies consider the time-reverse approach [*Schmalholz*, 2008; *Lechmann et al.*, 2010]. An

<sup>1</sup>Department of Geodynamics and Sedimentology, University of Vienna, Vienna, Austria.

<sup>2</sup>Now at Geological Institute, ETH Zurich, Zurich, Switzerland.

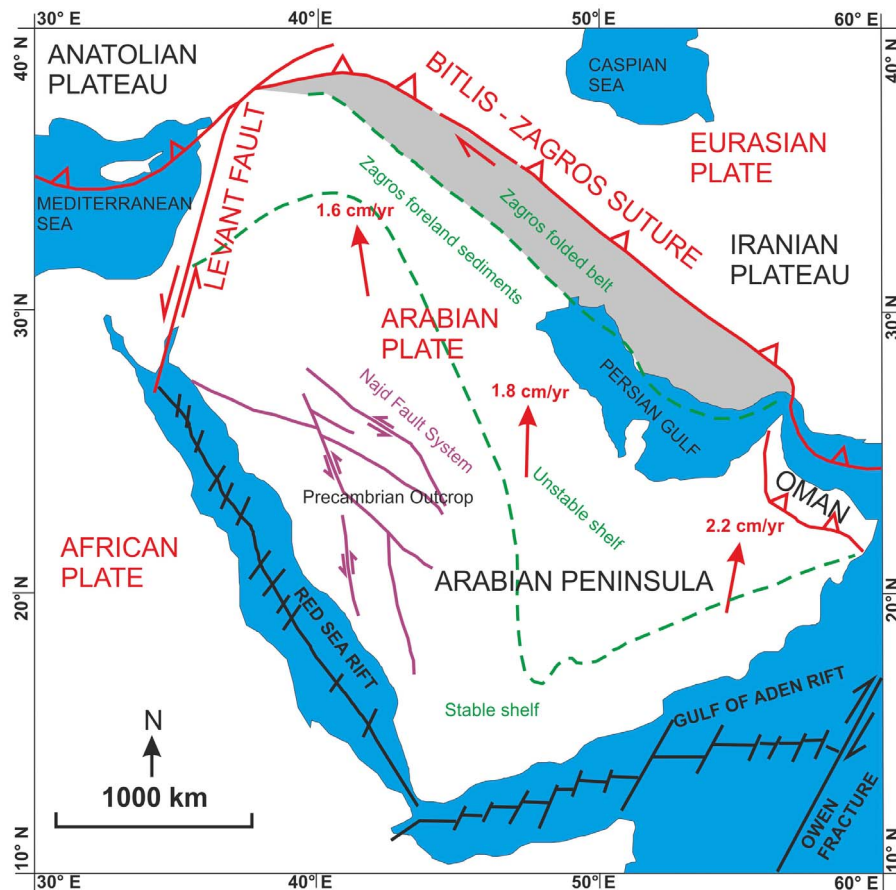


**Figure 1.** Tectonic overview of the Middle East. The plate velocities denoted by red arrows refer to the motion of the Arabian Plate with respect to the fixed Eurasian Plate and are based on GPS measurements by *Hessami et al.* [2006]. The Zagros folded belt, where the investigated area is situated, is shaded.

application of dynamic unfolding to natural folds has only been presented once by *Lechmann et al.* [2010], which shows that the method is still under development. Nevertheless, in this study the concept of dynamical unfolding is applied to a two-dimensional 55.5 km long cross section through the Zagros High Folded Zone in the Kurdistan Region of Iraq. The results are correlated with parameters derived from kinematical restoration (length- and area-balancing) of the same cross section. The chosen area of investigation is ideally suited for testing dynamical unfolding calculations because there is no evidence of significant faulting intersecting the folded profile, which has been confirmed by various seismic cross sections (H. Peresson, OMV Exploration and Production Company, personal communication, 2010).

## 2. Geological Setting

### 2.1. The Zagros Fold-and-Thrust Belt

[5] The Zagros Mountains (Figure 1) extend for about 1800 km in NW–SE direction and are bordered by the Central Iranian Plateau in the NE, the Taurus Mountain range in Turkey in the NW, the Oman Fault in the SE, and the Persian Gulf foreland in the SW [*Talbot and Alavi*, 1996], forming a

major segment of the Alpine-Himalayan Orogen. The orogeny started in the Upper Cretaceous, following the collision between the Arabian and Eurasian plates as a result of the closure of the Neotethys oceanic basin [*Berberian*, 1995; *Talbot and Alavi*, 1996]. The shortening between the Arabian and Eurasian plates, whose horizontal velocity still reaches 2–2.5 cm/a (Figure 1), is partitioned into S–SW directed folding and thrusting of the Tethyan sediments and NW–SE to N–S trending dextral strike slip faulting [*McQuarrie*, 2004]. The total convergence in the Zagros fold-and-thrust belt is  $70 \pm 20$  km, which represents 20% of the overall convergence between the Arabian and Eurasian plates [*McQuarrie*, 2004].

[6] Deposition of the 9–10 km thick sedimentary sequence, which rests on a Precambrian polymetamorphic basement [*Jassim and Goff*, 2006], started in the Upper Permian to Upper Triassic, reflecting continental rifting along NW–SE striking normal faults and the opening of the Neotethyan Ocean [*Alavi*, 2004, and references therein]. During the Cretaceous, NE directed subduction of the Neotethys started, followed by SW directed obduction of ophiolites and the uplift of the inner Zagros Orogen [*Hooper et al.*, 1995]. As a result of ongoing subduction the Neotethys closed in the Miocene. In the Pliocene to Pleistocene,

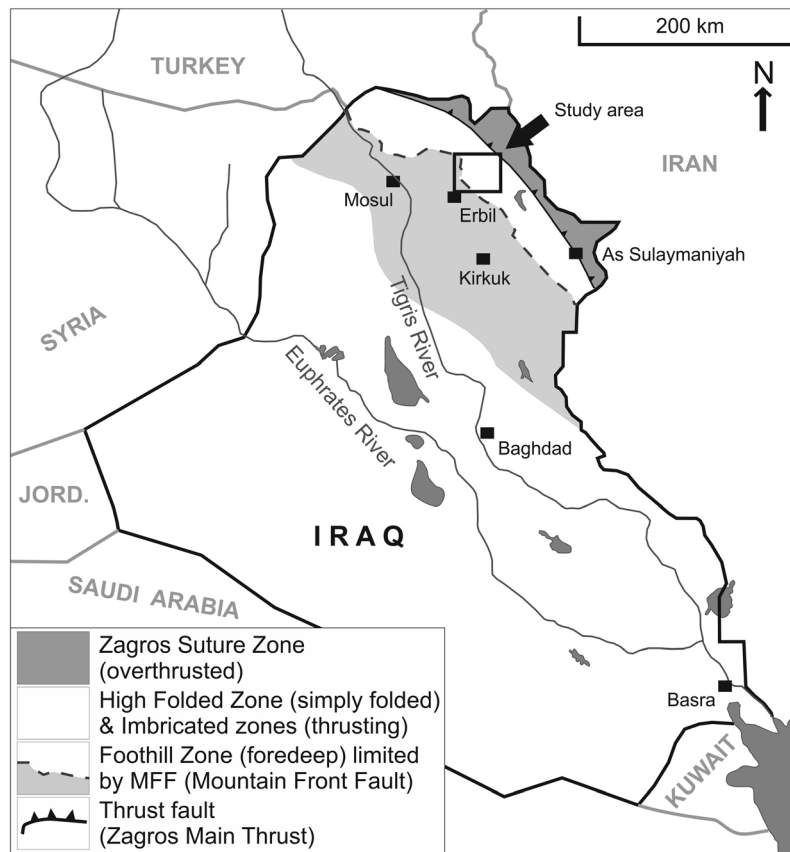


**Figure 2.** Position of the study area in the High Folded Zone of the Zagros fold-and-thrust belt.

continent-continent collision between the Arabian and Eurasian plates resulted in the main phase of the Zagros orogenic compression and the development of the fold-and-thrust belt [Homke *et al.*, 2004]. Basin inversion and reverse reactivation of Permian to Triassic normal faults resulted in the formation of small basins and local folding of the sediments [e.g., Numan *et al.*, 1998]. Today, the Zagros fold-and-thrust belt hosts about 50% of the fold-and-thrust belt-related, and more than 5% of the world's total hydrocarbon reserves [Cooper, 2007], mostly in anticlinal traps.

## 2.2. Tectonic Setting of the Study Area

[7] In the Kurdistan Region of Iraq the Zagros fold-and-thrust belt is divided into four NW–SE striking tectonic units as shown by Jassim and Goff [2006] (Figure 2): The Zagros Suture Zone, the Imbricated Zones, the High Folded Zone (equivalent to the Simply Folded Belt in the Iranian part of the Zagros as defined by Berberian [1995]), and the Foothill Zone. The boundary between the High Folded Zone and the Foothill Zone is marked by a regional morphotectonic feature, the Mountain Front Fault (Figure 2), delineated by a clustering of seismic events, which causes a sudden change in the level of exposed sedimentary layers. The Mountain Front Fault (Figure 2) is trending parallel to the Zagros Belt and is interpreted as a result of the reactivation of Zagros basement structures [Berberian, 1995; Jassim and Goff, 2006; McQuarrie, 2004]. In the study area (Figure 3) the NE–SW shortening is unevenly distributed, increasing from

the Foothill Zone in the SW (~5%) through the High Folded Zone (~15%) and the Imbricated Zones (up to 25%) to the Zagros Suture Zone in the NE.

[8] The Zagros fold-and-thrust belt in the Kurdistan Region of Iraq is dominated by open to gentle harmonic folding with amplitudes of less than 2.5 km and a characteristic wavelength of 5–10 km, which is considerably lower than the average values of 15–25 km in the SE part of the Zagros [Mouthereau *et al.*, 2007]. The two main reasons for this difference in fold wavelength are the absence of major faults and the absence of thick salt horizons. For example, the neo-Proterozoic Hormuz salt overlying the crystalline basement in the SE part of the Iranian Zagros, which acts as a ductile detachment during deformation [Mouthereau *et al.*, 2007], is absent in the NW part of the Zagros. Nevertheless, other, several meters thick detachment horizons within the cover rocks, for example Triassic evaporites, Cretaceous shales or Miocene evaporites, play an important role in the regional deformation and in the formation of the Zagros folds [e.g., Sepehr *et al.*, 2006]. Some of these weak layers locally translate into thicker horizons leading to a decoupling of the deformation between different units within the cover sequence, which may significantly influence the fold wavelength.

## 2.3. Lithostratigraphy

[9] The fold trains in the investigated area comprise Jurassic to Cenozoic sediments consisting mainly of limestone,

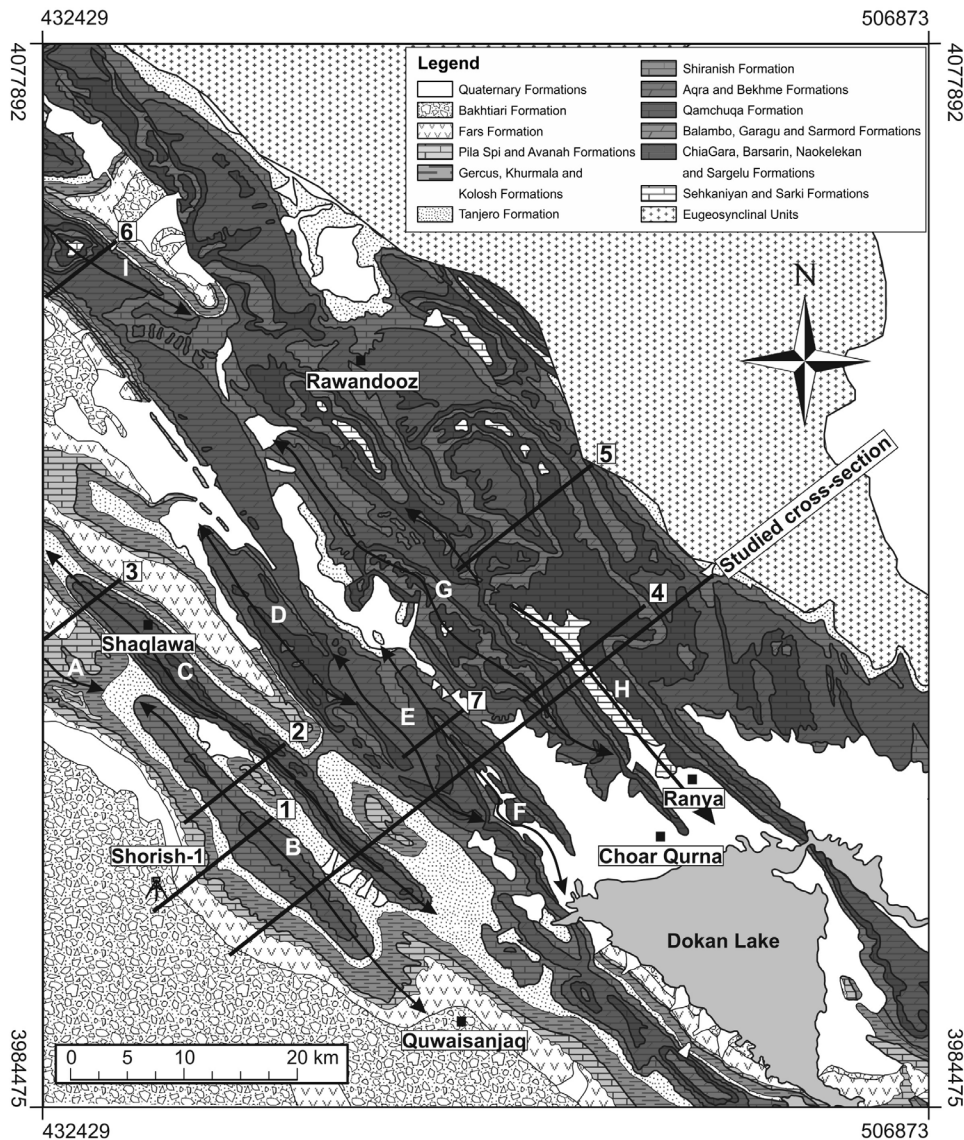


**Figure 3.** Geological map of the study area (modified from *Sissakian et al.* [1997]) with the positions of the 55.5 km long cross section (Figure 5) and several short balanced cross sections (1–7). Cross sections 2 and 3 are based on the same data as the cross sections of *Bretis et al.* [2011]. Shortening values are kinematically calculated from these cross sections as (1) 4.5%, (2) 14%, (3) 14%, (4) 15.3%, (5) 16.9%, (6) 14.6%, and (7) 13.5%. The studied anticlines are (A) Permam Anticline, (B) Bana Bawi Anticline, (C) Safeen Anticline, (D) Shak Rook Anticline, (E) Kamosk Anticline, (F) Pelewan Anticline, (G) Makook Anticline, (H) Ranya Anticline, and (I) Peris Anticline. Coordinates are in World Geodetic System (WGS) 84, universal transverse Mercator (UTM) 38N.

dolomite, sandstone, siltstone, claystone and conglomerate. In the Iranian part of the Zagros fold-and-thrust belt, *Sepehr et al.* [2006] noted that the mechanical anisotropy of the formations due to interlayering of relatively strong (massive dolomite and limestone) and weak (claystone, siltstone and shale) sediments (Figure 4a) strongly controls the style of folding. The terms “strong” and “weak” are used here to semiquantitatively describe the resistance of rocks to deformation in terms of their relative mechanical strength. Additionally, the folding is influenced by a few low-shear-strength layers that may act as interfacial slip surfaces (Figure 4b).

For example, the Miocene to Pliocene Lower Fars (also known as Fatha) Formation contains thin layers of claystone and evaporite (gypsum and anhydrite) and directly overlies the uppermost layer of the modeled cross section. Other possible interfacial slip surfaces are found in the Lower Jurassic Sehkaniyan and Sarki Formations [*de Vera et al.*, 2009], consisting mainly of limestone and dolomite, but also containing clay-rich and bituminous thin-bedded shales of low shear strength. Unfortunately, there is no control from the regional geology about the mechanical stratigraphy below the Lower Jurassic. In the absence of a thick

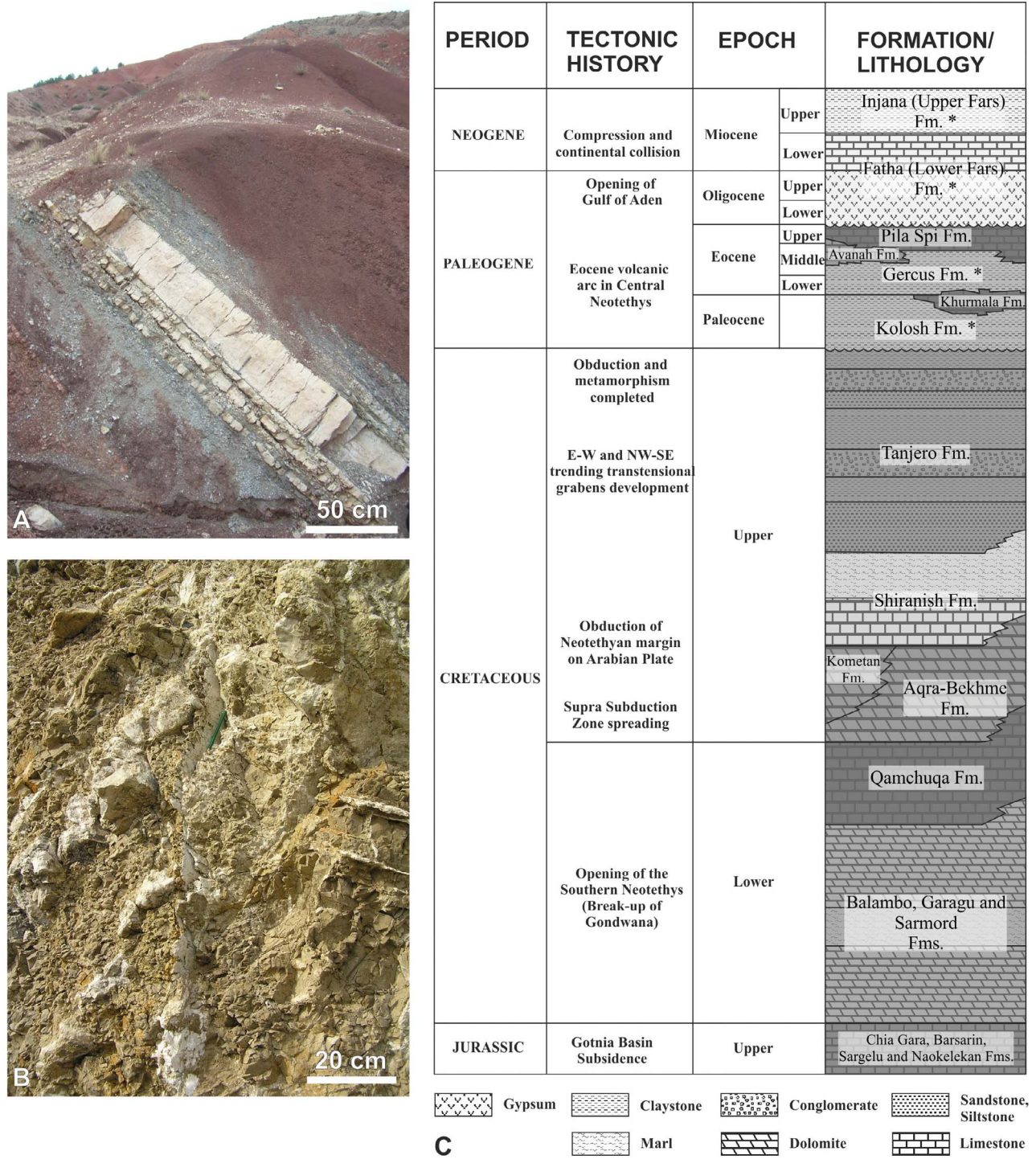


**Figure 4.** (a) The mechanically strong limestone bed interlayered within the thick, weak Gercus Formation claystones. Safeen Anticline, E 4,029,915 m, N 439,545 m, facing NW. (b) Detail of the Miocene to Pliocene Lower Fars (also known as Fatha) Formation containing layers of claystone and evaporite (gypsum and anhydrite) with low shear strength. Hareer Anticline, E 4,048,402 m, N 439,609 m, facing WNW. (c) Stratigraphic column modified from *Sissakian et al.* [1997] and divided according to the modeled units with low-shear-strength formations denoted by an asterisk.

**Table 1.** Lithology, Age, and Thickness of Formations in the Investigated Area by Unit<sup>a</sup>

Unit	Lithology	Age	Formations (Thickness, m)	Unit Thickness (m)
8	Well-bedded limestone	Eocene	Pila Spi (120), Avanaah (180)	300
7	Black claystone, siltstone, limestone, red sandstone, claystone	Paleocene–upper Eocene	Gercus (80), Khurmala (105), Kolosh (400)	585
6	Khaki siltstone and claystone with conglomerate	Upper Cretaceous	Tanjero (300)	300
5	Well-bedded limestone, blue marl	Upper Cretaceous	Shiranish (280)	280
4	Well-bedded to massive limestone (marly limestone)	Upper Cretaceous	Kometan (20), Aqra-Bekhme (180)	200
3	Massive limestone, dolomite	Lower Cretaceous	Qamchuqa (660)	660
2	Marly limestone, marl, bedded limestone, dolomite	Lower Cretaceous	Lower Balambo (170), Lower Sarmord (110)	280
1	Mainly bedded to massive dolomite, limestone, marl	Upper Jurassic	Chia Gara (230), Barsarin (80), Naokelekan/Sargelu (150), Sehkanian (170)	630
Cross-section thickness:				3235

<sup>a</sup>Average thickness and lithology according to *Sissakian et al.* [1997]. Unit 7 is mechanically weak.

detachment layer above the crystalline basement, *Vergés et al.* [2011] have recently presented a conceptual model for the NW Zagros, where the space in the core of anticlines is accommodated by a number of thrust wedges forming from interfacial slip surfaces.

[10] There are evidences, however, that the folds developed at the surface. The Upper Miocene/Pleistocene Bakhtiari Formation, which comprises gravel sandstones, conglomerates, and red mudstones, is the youngest formation involved in the folding in the investigated area. The sediments record characteristic fanning growth stratal wedges on both limbs of the folds and are partly tilted by ongoing limb rotation. Therefore, the folds formed during deposition of the Bakhtiari Formation at the Earth's surface with no upper detachment horizon. This has important implications for the dynamic unfolding simulations, as no upper detachment has to be incorporated into the numerical model. Erosion during folding might influence the fold amplification rate, which is however not incorporated in the numerical model. In the following, the lithostratigraphic formations found in the cross section are described in detail from the oldest to the youngest formation and are summarized in Table 1 and Figure 4c:

[11] *Unit 1.* Starting in the Middle Jurassic, the formations Sehkanian, Naokelekan/Sargelu, Barsarin, and Chia Gara are grouped into one strong unit. The thicknesses of the different formations in the study area are: Sehkanian ~170 m, Naokelekan/Sargelu ~150 m, Barsarin ~80 m, and Chia Gara ~230 m, resulting in a total thickness of 630 m. The Sargelu Formation is a thin-bedded, blackish, bituminous and dolomitic limestone containing black shales and streaks of thin black chert. The Naokelekan Formation comprises three units: the lower unit consisting of laminated argillaceous bituminous limestone alternating with shale and fine-grained limestone; the middle unit consisting of thin-bedded dolomitic limestone; and the upper unit consisting of thin-bedded bituminous dolomite and limestone with black shale beds in the lower parts. The Barsarin Formation consists of limestone and dolomitic limestone, which is locally rich in

chert. The Chia Gara Formation comprises thin-bedded limestone and calcareous shale.

[12] *Unit 2.* This mechanically strong unit groups the formations of the Lower Cretaceous, namely the Lower Sarmord, and the Balambo Formations with an overall thickness of 280 m. The Lower Sarmord with a thickness varying from 100 to 250 m comprises bluish and brown marls with beds of argillaceous limestone. The Balambo Formation consists of thin-bedded limestone with dark layers of green marl and dark blue shale. There is no evidence of Balambo Formation in the boreholes Shorish-1 (Figure 2) NE of Erbil (H. Peresson, OMV Exploration and Production Company, personal communication, 2010).

[13] *Unit 3.* This unit consists of the strong Lower Cretaceous Qamchuqa Formation with a thickness varying between 600 and 800 m. The formation comprises detrital and argillaceous limestones, which are partly dolomitized. The thickness of the Qamchuqa Formation in the studied cross section is 660 m.

[14] *Unit 4.* With a thickness of 200 m, the Upper Cretaceous Aqra-Bekhme Formation and locally the Kometan Formation (thin-bedded grey limestone with chert concretions) represent the mechanically strong Unit 4. Although the Kometan Formation reaches a thickness of up to 500 m [*Jassim and Goff*, 2006] it is only 20 m thick in the borehole Shorish-1 (H. Peresson, OMV Exploration and Production Company, personal communication, 2010). The Aqra-Bekhme Formation comprises massive dolomitized limestone locally impregnated with bitumen.

[15] *Unit 5.* The Upper Cretaceous Shiranish Formation defines Unit 5 with a thickness of ~280 m. It comprises thin-bedded marly limestone with high pyrite content (Lower Shiranish) and blue pelagic marls (Upper Shiranish). Toward NE, this formation gradually passes into the Tanjero Formation [*Jassim and Goff*, 2006].

[16] *Unit 6.* The overlying mechanically strong Upper Cretaceous Tanjero Formation has not been found in the borehole Shorish-1 (Figure 2) (H. Peresson, OMV Exploration and Production Company, personal communication,

2010), but has been mapped in the investigated area [Sissakian *et al.*, 1997]. The thickness of the formation in Kurdistan is very variable, reaching locally 2000 m [Jassim and Goff, 2006]. In the studied cross section, the Tanjero Formation is 300 m thick. The lower part consists of claystones with conglomerate layers and the upper part consists of siltstone beds.

[17] *Unit 7.* This unit comprises three different mechanically weak formations, Kolosh, Khurmala and Gercus, with significantly different mechanical behavior and a bulk thickness of 585 m. The oldest two formations, Kolosh and Khurmala, are of Paleocene age. The Kolosh Formation is about 400 m thick in the cross section, but only about 300 m in the close-by Kirkuk-117 borehole [Jassim and Goff, 2006]. In the field, the Kolosh Formation shows evidences of shear deformation between the underlying Cretaceous limestones and the overlying strong Unit 8 (Avanah and Pila Spi limestones). This clastic formation comprises black claystone and shale with thin limestone beds occurring at the top of the formation. The calcareous beds of the Paleocene Khurmala Formation are interfingering or overlie the Kolosh Formation. The middle–upper Eocene Gercus Formation comprises molasse sediments deposited after the middle Eocene surface uplift [Jassim and Goff, 2006] and contains red sandstone and claystone with some thin-bedded limestone and gypsum layers.

[18] *Unit 8.* This 300 m thick mechanically strong unit contains the Pila Spi and Avanah Formations with a thickness of 120 and 180 m, respectively. The Pila Spi Formation is a well-bedded middle–upper Eocene limestone sandwiched between the underlying Gercus and the overlying Lower Fars Formations, both of which are less resistant to weathering. Therefore, the Pila Spi Formation frequently develops topographic ridges throughout the Zagros High Folded Zone. In the investigated area the nummulitic Eocene Avanah Formation underlies the basal part of the Pila Spi Formation [Jassim and Goff, 2006].

## 2.4. Structural Style

[19] Overall, the intensity of deformation increases northeastward (Figure 3) from the Persian Gulf foreland, where strata are not deformed and lie horizontally, to the Zagros High Folded Zone, which is characterized by double plunging subcylindrical folds [Burtscher *et al.*, 2012], gentle to open in the SW and close to locally SW overturned in the NE. The intensity of deformation continues to increase further to the NE, where thrust faulting is dominant in the Imbricated Zones. This deformation pattern suggests that the deformation front has migrated through time from the NE to its present position approximately in the center of the Persian Gulf foreland [Alavi, 1994]. The sedimentary column in the studied region has a total thickness of 9–10 km and at least parts of the Mesozoic and the Cenozoic sediments have been folded without evidences of major thrusting. The individual layers feature some mechanical strength differences relative to each other (Figure 4a). On a local scale, shortening is accommodated in the inner arc of the neutral surface by SW and NE directed blind thrusts with a strong displacement gradient and maximum offsets of less than a few tens of meters. Occurrence of S- and Z-shaped higher-order folds have only been observed in weaker layers, where evidences for shear deformation, for example SCC'-like

geometries [Passchier and Trouw, 2005] or layer-parallel slickensides are locally preserved. They originate from shearing caused by the relative displacement between the strong limestone layers (i.e., flexural slip folding) that control the deformation.

[20] A large number of thin mechanically weaker layers between the thick strong units, as in the case of the Upper Shiranish Formation (interlayering of blue marl and limestone), favors the development of asymmetric higher-order folds, because they have a larger amplification rate and thus require less shortening to develop [Frehner and Schmalholz, 2006].

## 3. Balanced Cross Sections

### 3.1. Derivation of Dip Domains

[21] More than 2000 measurements of bedding orientations and fracture systems were taken in the Zagros High Folded Zone during field studies [Bretis *et al.*, 2011; Reif *et al.*, 2011], mostly from road cuts. Although security in this part of the Zagros Mountains is much better than elsewhere in Iraq, off-road access was severely restricted due to contamination of the area with landmines and unexploded ordnance. Thus only a few short cross sections, mostly along main roads oriented perpendicular to the trend of the fold axes, could be measured (Figure 3) [Bretis *et al.*, 2011; Reif *et al.*, 2011].

[22] Dip directions and dip angles of the limbs of several anticlines were measured in detail (Figure 3) and a 55.5 km long profile across seven anticlines was constructed (Figure 5). Except for the symmetric and upright Permian Anticline, the measured folds show a clear asymmetric SW vergence, with steeper SW dipping forelimbs and shallower NE dipping backlimbs (Figure 5). To complement structural measurements from the field campaign and to fill measurement gaps in inaccessible areas, remote sensing techniques were developed for extracting the sedimentary bedding orientation from the 15 m horizontal and 8 m vertical resolution ASTER (Advanced Spaceborne Thermal Emission and Reflection Radiometer) digital elevation model [Reif *et al.*, 2011]. Due to differences in erosion resistance, the more resistant lithologies form sharp ridges with steeply sloping sides along the eroded flanks of the anticlines [Bretis *et al.*, 2011]. These hogbacks, up to several 100 m high, form triangular shaped flanks outlining the dip of the strata and can easily be identified in the digital elevation model [Burtscher *et al.*, 2012].

### 3.2. Construction of Kinematically Balanced Cross Section

[23] For the profile construction (Figure 5), the constant dip domain method was used [Tearpock and Bischke, 2003]. This method separates domains of similar dip angles across a folded region by axial planes bisecting the dip angle between neighboring domains. By including the lithological boundaries mapped at the surface and assuming that the surface dip of the bedding also reflects the dip of the underlying sediments, a line- and area-balanced cross section has been constructed (Figure 5). The thickness of some formations (Table 1) is not very well constrained and was estimated from surface outcrops, borehole information in the area, and literature data [Jassim and Goff, 2006]. The resulting bulk

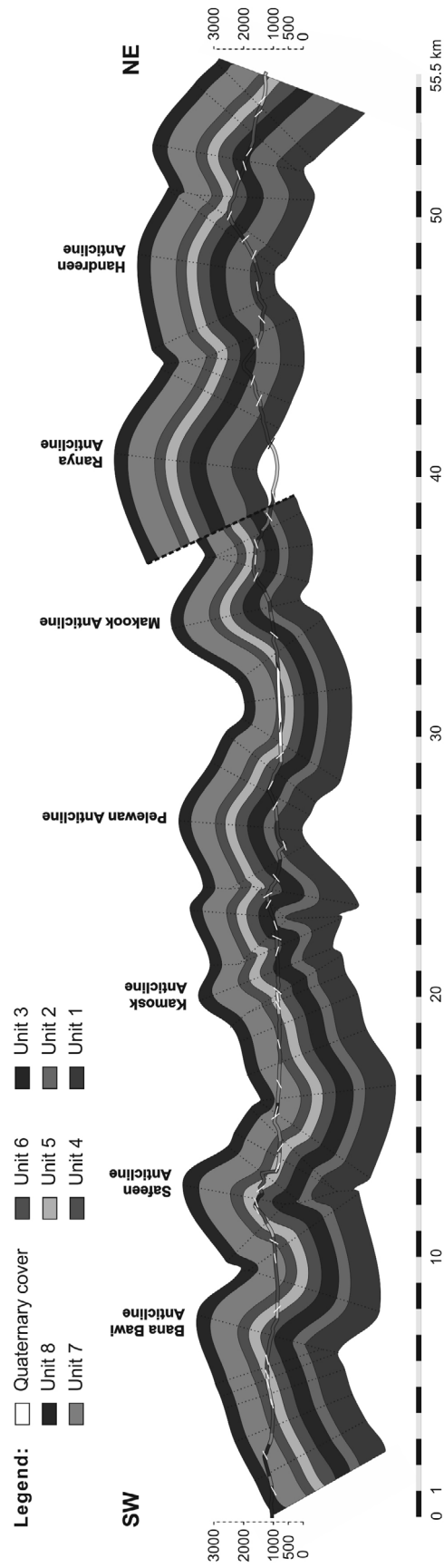


**Figure 5.** Balanced cross section constructed from field and remote sensing data using the dip domain method. The lithology of the various units is shown in Figures 3 and 4c, and the location of the cross section is shown in Figure 3. The offset of the thrust fault in the NE part of the profile is unknown.

**Table 2.** Material Parameters for Dynamic Unfolding Simulations<sup>a</sup>

Simulation	Rheology	Layers 1–6 and 8 (Mechanically Strong)	Layer 7 (Mechanically Weak)	Interfaces Between Layers	Layers Above and Below Layer Stack
<i>No Basement</i>					
1	Newtonian	$\eta = 100$	$\eta = 1$	welded	$\eta = 1$
2	Newtonian	$\eta = 100$	$\eta = 1$	$\eta = 1$	$\eta = 1$
3	Newtonian	$\eta = 100$	$\eta = 1$	$\eta = 0.1$	$\eta = 1$
4	Power law viscous	$\eta_0 = 100, n = 1$	$\eta_0 = 1, n = 3$	$\eta_0 = 1, n = 3$	$\eta_0 = 1, n = 3$
5	Power law viscous	$\eta_0 = 100, n = 3$	$\eta_0 = 1, n = 1$	$\eta_0 = 1, n = 1$	$\eta_0 = 1, n = 1$
6	Power law viscous	$\eta_0 = 100, n = 3$	$\eta_0 = 1, n = 3$	$\eta_0 = 1, n = 3$	$\eta_0 = 1, n = 3$
<i>Basement</i>					
7	Newtonian	$\eta = 100$	$\eta = 1$	$\eta = 1$	$\eta = 1, d = 10.9$ km
8	Newtonian	$\eta = 100$	$\eta = 1$	$\eta = 1$	$\eta = 1, d = 7.0$ km
9	Newtonian	$\eta = 100$	$\eta = 1$	$\eta = 1$	$\eta = 1, d = 3.1$ km
10	Newtonian	$\eta = 100$	$\eta = 1$	$\eta = 1$	$\eta = 1, d = 1.2$ km
11	Power law viscous for $d = 3.1$ km	$\eta_0 = 100, n = 1$	$\eta_0 = 1, n = 3$	$\eta_0 = 1, n = 3$	$\eta_0 = 1, n = 3$
12	Power law viscous for $d = 3.1$ km	$\eta_0 = 100, n = 3$	$\eta_0 = 1, n = 1$	$\eta_0 = 1, n = 1$	$\eta_0 = 1, n = 1$

<sup>a</sup>Here,  $\eta$ , dimensionless dynamic viscosity for Newtonian rheology (using viscosity of layer 7 as characteristic viscosity);  $\eta_0$ , dimensionless reference dynamic viscosity for power law viscous rheology (using viscosity of layer 7 as characteristic viscosity);  $n$ , power law exponent for power law viscous rheology;  $d$ , basement depth below layer 1.

thickness of the cross section is 3235 m. The cross section only contains one major fault in the NE part between the Ranya and Makook Anticlines (Figure 5). This fault is likely to be a part of a NW–SE oriented fault zone, which may connect with the High Zagros Fault dividing the Imbricated Zones from the High Folded Zone [Casciello *et al.*, 2009].

[24] In the SW of the cross section the first major anticline emerging from the foreland is the Bana Bawi Anticline (Figure 5). The forelimb is dipping with  $\sim 25^\circ$  toward SW. According to field measurements, the backlimb has a mean dip of  $\sim 45^\circ$  toward NE. The Bana Bawi Anticline is separated by a narrow syncline from the Safeen Anticline, whose forelimb has a mean dip of  $\sim 60^\circ$  toward SW. A broad syncline with a mean dip of both limbs of  $\sim 27^\circ$  separates the SW verging Kamosk Anticline and the slightly NE verging Pelewan Anticline. Between the latter and the adjacent SW verging Makook Anticline there is again a broad syncline with  $\sim 25^\circ$  mean dip of both limbs. Between the Makook backlimb (mean dip of  $\sim 30^\circ$ ) and the Ranya Anticline a thrust marks the border between the High Folded Zone and

the Imbricated Zones. The exact location, the dip angle and the offset of this NW dipping thrust are unknown because no outcrops have been found in the field.

## 4. Dynamical Unfolding of the Cross Section

### 4.1. From Cross Section to Model

[25] To perform dynamical unfolding simulations several steps are necessary to transform the two-dimensional profile (Figure 5) into a numerical finite element model:

[26] 1. Choose an appropriate part of the profile. For practical reasons, only the part of the profile is used that is not intersected by faults.

[27] 2. Cut profile at fold axial planes. The numerical model uses vertical traction-free boundary conditions at both ends of the folded profile. Therefore, the profile is cut at positions where vertical tractions are expected to be smallest, which is along fold axial planes.

[28] 3. Assign rheology and material parameters. This is probably the most difficult step, because the material

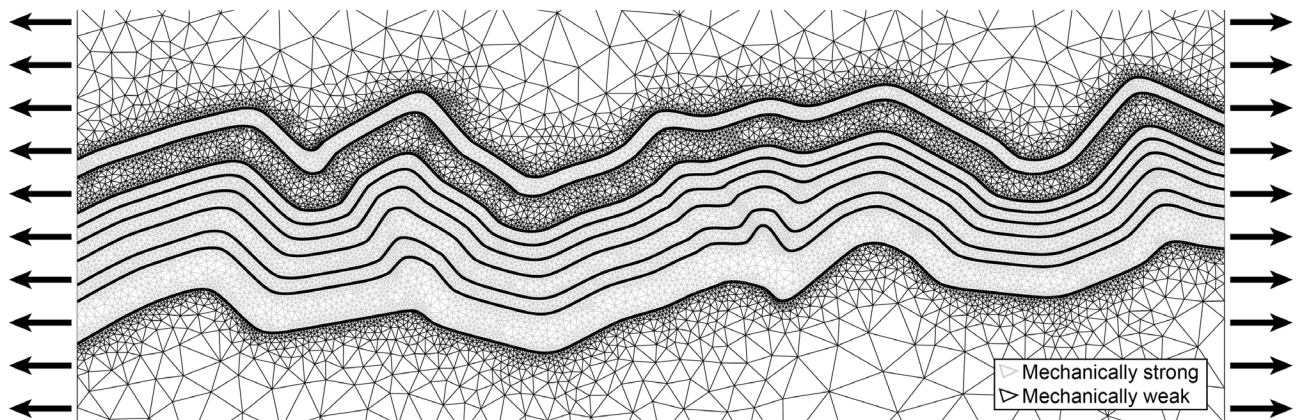


**Figure 6.** Initial model setup and triangular finite element mesh for the dynamical unfolding simulations. For interfacial slip conditions, thin weak layers are introduced at the layer boundaries. The top and bottom boundaries are far enough away from the layer stack to avoid boundary effects. For simulating a detachment, the bottom boundary is close to the layer stack (see text for more details).

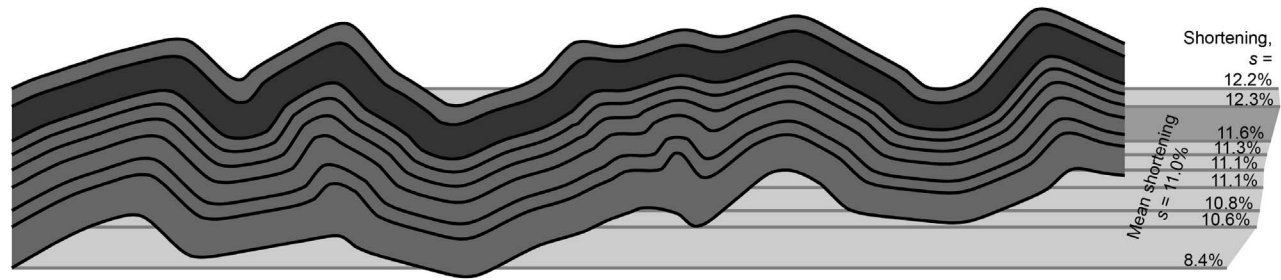


**Figure 7.** Kinematical unfolding (constant arc length) of the part of the folded profile that is used for the dynamical unfolding simulations.

behavior of the modeled rock units is not known from laboratory testing. Therefore, rheological flow laws and the corresponding material parameters have to be assigned based on field observations and comparison with similar lithologies from the literature [e.g., Vanoni, 2006].

[29] The goal of this study is to investigate first-order effects and, as suggested by *Lechmann et al.* [2010], to indicate which areas future field work should focus on. Therefore, a relatively basic incompressible power law viscous rheology (power law exponent,  $n$ ) is used for all layers [Fletcher, 1974; Frehner, 2011]. This is at the same time the most complex rheology to date, for which dynamical unfolding has been successfully tested in synthetic cross sections [Lechmann et al., 2010]. More complex rheologies, such as plasticity or viscoelasticity, first need to be tested for their applicability in reverse time simulations before they can be used with confidence in dynamical unfolding simulations. If the power law exponent,  $n$ , is set to 1, the rheological behavior is incompressible linear viscous (Newtonian). Based on the field investigations (Figures 4 and 5 and Table 1), only Unit 7 could be identified as mechanically weak (Table 2). Two fundamentally different conditions for the interfaces between the different units were tested: (1) perfectly welded layer interfaces and (2) interfacial slip between the layers. This interfacial slip condition is modeled by introducing thin weak layers at the layer interfaces (Table 2). The resulting initial model setups for the dynamical unfolding simulations are shown in Figure 6; material parameters are given in Table 2.

[30] The finite element method is used to solve the force balance equations in two dimensions for incompressible Newtonian and/or power law viscous materials. The profile is discretized with an unstructured mesh using triangular elements (Figure 6). The particular code used here is described in detail and applied to fold development by *Frehner and Schmalholz* [2006] (Newtonian) and *Frehner* [2011] (Newtonian and power law viscous). For numerically unfolding the profile, extensional traction-free boundary conditions were applied at the left and right boundaries (Figure 6) by adjusting the horizontal velocity every time step to maintain a constant bulk rate of horizontal extension. At the bottom and top boundaries, traction-free boundary conditions and free surface boundary conditions were applied, respectively. However, these two boundaries were set far enough away from the layer stack to minimize boundary effects. The space above and below the layer stack was defined as mechanically weak (Figure 6 and Table 2).

[31] Prior to the dynamical unfolding simulations the same part of the folded profile was kinematically unfolded (Figure 7) by assuming a constant length of the individual layer interfaces and no layer-parallel shortening or extension during folding. By comparing the original length,  $L_0$ , and the unfolded length,  $L$ , of the profile the elongation of the unfolding,  $e$ , can be calculated as

$$e = (L - L_0)/L_0. \quad (1)$$

[32] From this value the horizontal shortening,  $s$ , can be calculated that transforms the unfolded geometry back into the folded profile, i.e.,

$$s = -(L_0 - L)/L = e/(1 + e). \quad (2)$$

[33] It is important to note that unfolding calculations (kinematical and dynamical), and therefore also the elongation value,  $e$ , represent a reverse time calculation. However, in the following, only the shortening,  $s$ , is considered because it represents the corresponding forward time history and is geologically much more relevant. In Figure 7, the calculated shortening differs for the different layer interfaces and ranges between 8.4% and 12.3%, with an average value of 11.0%.

#### 4.2. Rheology and Interface Condition

[34] Dynamical unfolding simulations were performed up to a shortening of 11.0% (i.e., kinematical constant arc length estimate) ignoring the effect of a basement. The results of six simulations using different rheological parameters and different interlayer conditions are shown in Figure 8 and correspond to the first six entries in Table 2. The two different interlayer conditions, welded and interfacial slip, but using otherwise identical model setups, result in markedly different profile geometries (Figures 8a and 8b, respectively). Allowing for interfacial slip (Figure 8b) leads to a much more efficient dynamical unfolding compared to the case of welded interfaces (Figure 8a), as can be seen by the flat-lying layers in a large portion of the profile. During the dynamical unfolding simulations the evolution of the average fold amplitude is calculated. The mean amplitude decrease (MAD) is a measure for the efficiency of the unfolding simulation and is defined as

$$\text{MAD} = -(A - A_0)/A_0, \quad (3)$$

where  $A$  is the unfolded average amplitude and  $A_0$  is the original average amplitude of the profile. The average

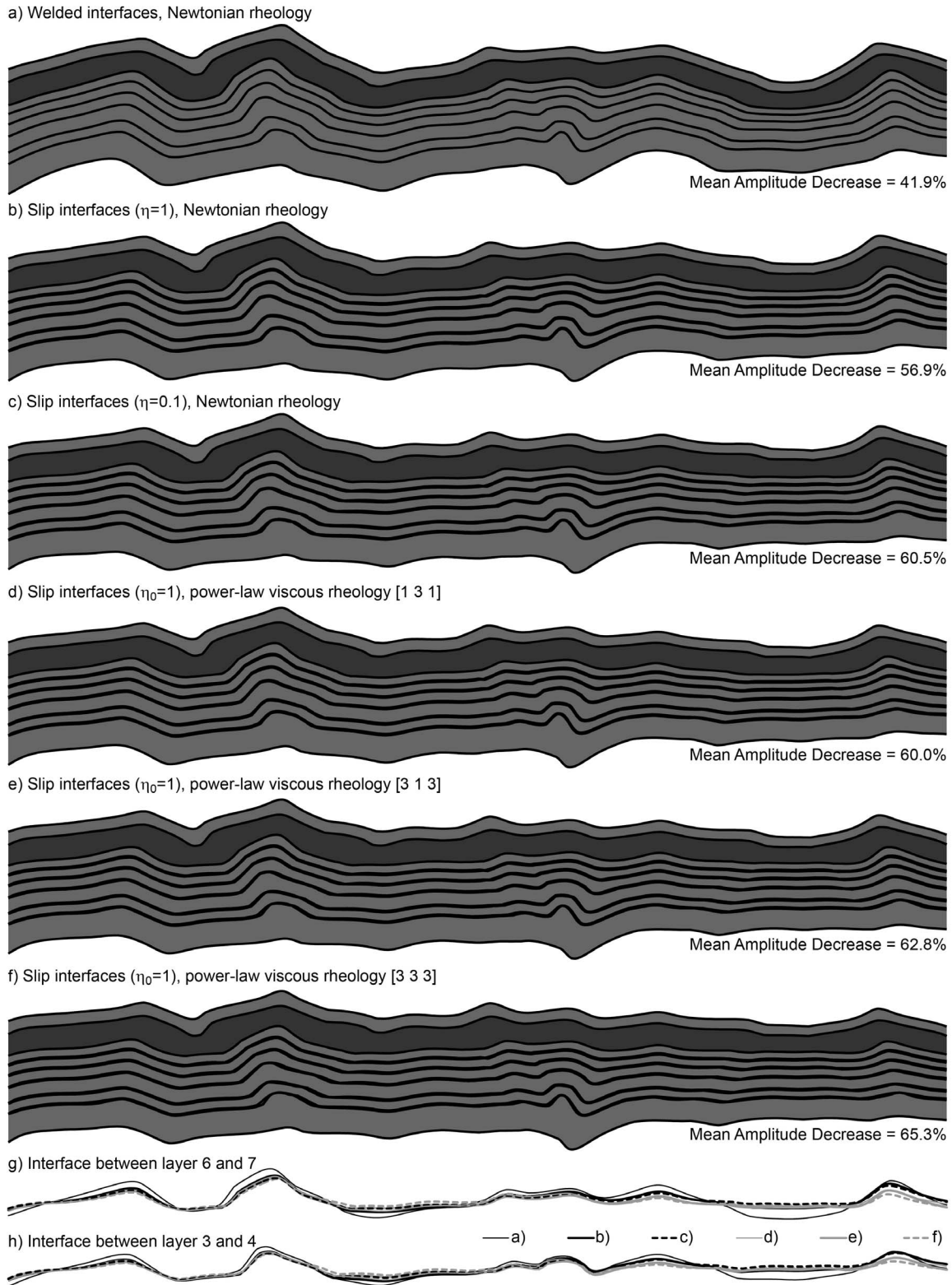


**Figure 8.** Dynamical unfolding simulations for a horizontal shortening of 11.0% and no basement. Figures 8a–8f correspond to the first six simulations listed in Table 2. For a better comparison between the different simulations, the interfaces between layers 6 and 7 and between layers 3 and 4 are overlain in Figures 8g and 8h, respectively.

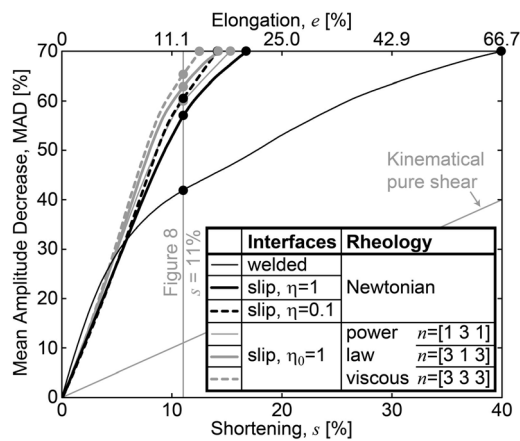


**Figure 9.** Mean amplitude decrease during the different progressive dynamical unfolding simulations without basement. The legend corresponds to the first six entries in Table 2. The thick black line is the same as the thick black line in Figure 10. Kinematical pure shear is equivalent to a dynamical unfolding simulation with no mechanical difference between the layers ( $MAD = s$ ).

amplitude is calculated as the arithmetic mean of the amplitudes of all the layer interfaces. The MAD is 56.9% in the case of interfacial slip (Figure 8b) and only 41.9% in the case of welded interfaces (Figure 8a), which confirms the more efficient dynamical unfolding in the case of interfacial slip compared to welded interfaces. Interfacial slip is made even more efficient in Figure 8c by lowering the relative viscosity of the thin weak interlayers by a factor 10, making them 1000 times weaker than the strong layers. This leads to an even more efficient unfolding simulation, as it is expressed by a larger MAD value of 60.5%.

[35] Figures 8d–8f show the dynamically unfolded profiles for three different power law viscous rheological parameter sets using a power law exponent of 1 and 3 (see also Table 2). The dynamical unfolding is equally or slightly more efficient as in the Newtonian case for interlayers 1000 times weaker than the strong layers (Figure 8c). MAD values range from 60.0% to 65.3%, whereas the highest value corresponds to the case where all layers have a power law exponent,  $n$ , equal to 3.

[36] Because a purely visual comparison between the different dynamical unfolding simulations in Figure 8 is difficult, Figure 9 depicts the evolution of the MAD during progressive unfolding for the different unfolding calculations. In the initial stage, up to a shortening of about 6%, all dynamical unfolding simulations show a similar fast decrease of the average amplitude. After that, all simulations with interfacial slip conditions evolve very differently than the simulation with welded layer interfaces. The MAD in the case of welded interfaces slows down significantly and the rate of the MAD (i.e., slope in Figure 9) is comparable to that of the kinematical pure shear unfolding calculation. At the same time, the rates of the MAD of all simulations with interfacial slip stay high. A MAD of 70% is reached already after a shortening of less than 17% while in the case of welded interfaces, this value is reached only after a shortening of 40.0%. In other words, much more shortening is

necessary to reach the same MAD as in the case of interfacial slip. Figure 9 suggests that the most important factor for an efficient dynamical unfolding is whether the layer interfaces are welded or slipping. Different Newtonian interfacial slip conditions or various power law viscous rheologies modify the results only marginally.

**4.3. Basement Influence**

[37] Several dynamical unfolding simulations were performed including a basement at various depths (Table 2). For these simulations a Newtonian rheology and interfacial slip conditions were chosen, because interfacial slip was recognized above as an important factor for an efficient unfolding. The basement is assumed to deform homogeneously without folding (or unfolding). Therefore, the basement deformation is not modeled explicitly, but the lower model boundary is set close to the layer stack of the cross section with boundary conditions equal to zero vertical displacement and homogeneous horizontal stretching, i.e.,  $v_x = \dot{\epsilon}x$ , where  $v_x$  is the horizontal velocity,  $\dot{\epsilon}$  is the extensional strain rate (the same as on the left and right boundaries), and  $x$  is the horizontal coordinate value at the lower boundary.

[38] Figure 10 shows the evolution of the MAD during progressive unfolding for the different dynamical unfolding simulations with a basement corresponding to the second and seventh to tenth entry in Table 2. The basement depth,  $d$ , is measured down from the lowest point of Unit 1 in the folded cross section. From Figure 10 it is clear that the rate of MAD is lower the closer the basement is to the layer stack. This observation can be qualitatively understood, because for a single-layer folding process it has been shown by *Schmalholz et al.* [2002] that the fold growth rate is smaller if a detachment is present. The same is true for the

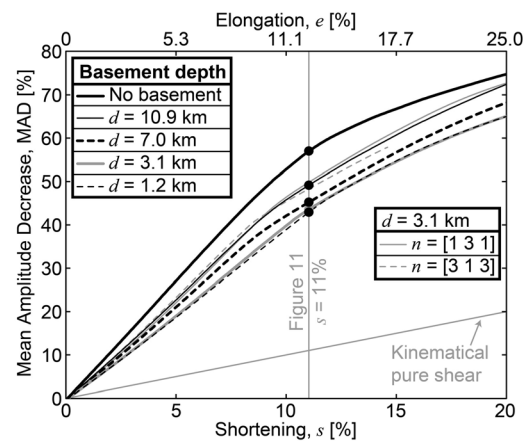


**Figure 10.** Mean amplitude decrease during different progressive dynamical unfolding simulations including a basement at depth  $d$ . The two legends correspond to the second and the last six entries in Table 2. The legend in the top left corner corresponds to simulations using a Newtonian rheology. The second legend corresponds to simulations using power law viscous rheologies. The thick black line is the same as the thick black line in Figure 9. Kinematical pure shear is equivalent to a dynamical unfolding simulation with no mechanical difference between the layers ( $MAD = s$ ).

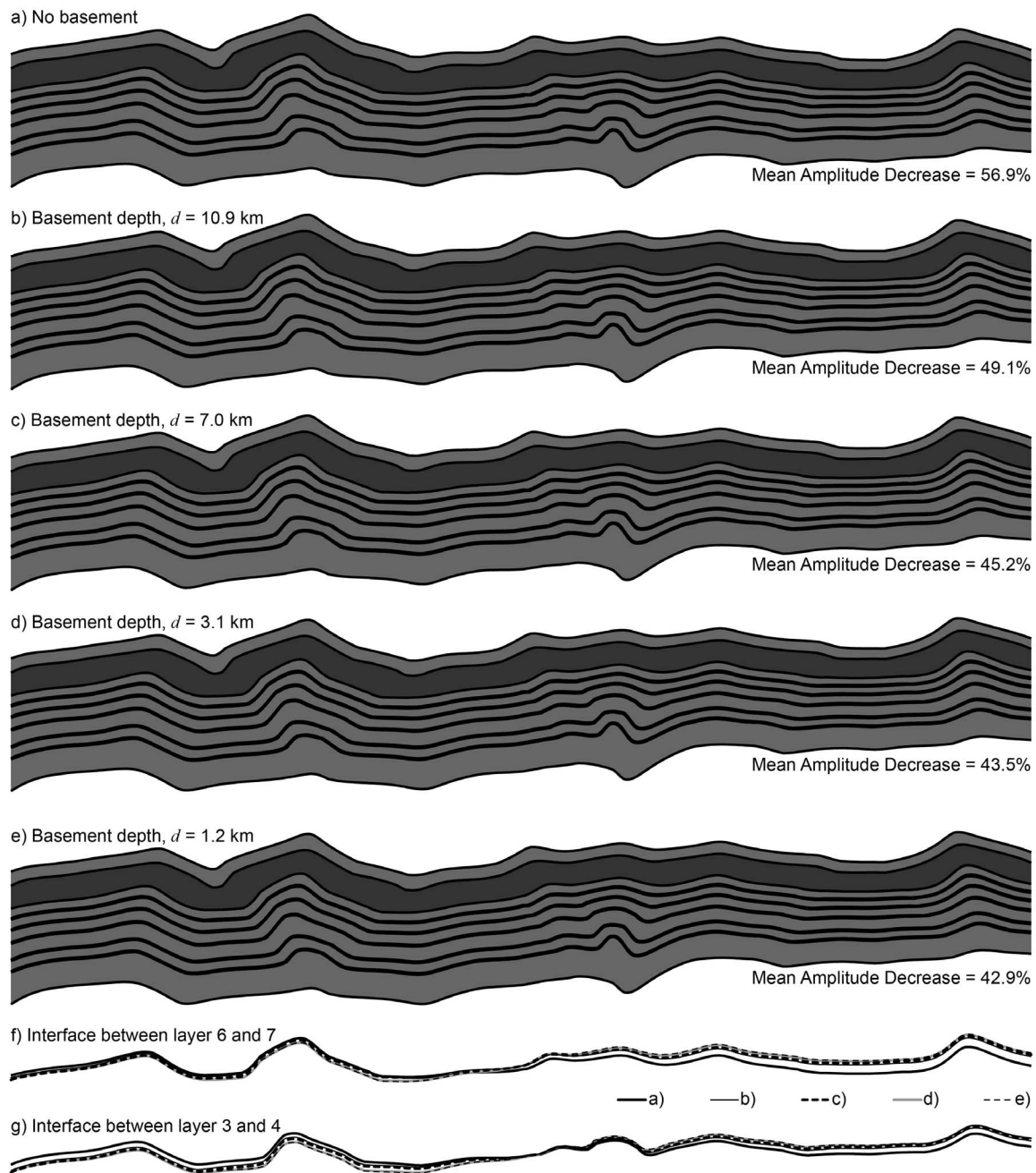


**Figure 11.** Dynamical unfolding simulations for a horizontal shortening of 11.0% and including a basement at depth  $d$ . Figures 11a–11e correspond to the second and seventh to tenth entries in Table 2. For a better comparison between the different simulations, the interface between layers 6 and 7 and between layers 3 and 4 are overlain in Figures 11f and 11g, respectively.

dynamical unfolding simulations, which become less efficient for a detachment close to the layer stack. The cross sections after dynamical unfolding of up to 11.0% (kinematical constant arc length estimate; dots in Figure 10) are shown in Figure 11. Even though the differences in the cross sections are small, it can be recognized that the amplitudes in the case without basement (Figure 11a) are reduced more than in the other cases. This is confirmed by the large MAD value of 56.9%. For all cases including a basement this value is lower

than 50%. In other words, the dynamical unfolding is less efficient in the presence of a basement.

[39] Two dynamical unfolding simulations were performed using power law viscous rheology with a power law exponent of  $n = 3$  in either the mechanically strong or the mechanically weak layers and for a basement depth of  $d = 3.1$  km. The two resulting MAD curves during progressive unfolding are also shown in Figure 10. The power law rheology increases the rate of MAD (i.e., slope in

Figure 10) compared to the simulation using a Newtonian rheology, and the MAD reaches a value between 48% and 50% at a shortening of  $s = 11\%$ . These values as well as the entire MAD evolution curves are very similar to the simulation using a Newtonian rheology but a larger basement depth of  $d = 10.9$  km. This indicates that in the presence of a basement a power law viscous rheology enhances the efficiency of the dynamic unfolding stronger than in the absence of a basement (Figure 9).

## 5. Discussion

[40] From kinematical fold restoration calculations in Iran it is generally believed that the Zagros Simply Folded Belt accumulated a horizontal shortening ranging from 7.5% to 17% (Figure 7) [also *Sherkati et al.*, 2006; *Molinario et al.*, 2005; *Mouthereau et al.*, 2007]. For a shortening of less than 17%, the dynamical unfolding simulations using interfacial slip between the layers exhibit a substantial fold amplitude decrease of 70% or more (Figure 9). For the same shortening value, the MAD for welded layer interfaces is only around 45% (Figure 9). In other words, interfacial slip provides more realistic modeling results and is the most important factor for an efficient unfolding of the cross section (more important than complex rheologies or the presence of a basement). A similar conclusion was drawn by *Yamato et al.* [2011] in the Iranian part of the Zagros fold-and-thrust belt, where a thick layer of Hormuz Salt [*Kent*, 1979; *Bahrudi and Koyi*, 2003] acts as a ductile detachment below the folded sedimentary layer stack. In contrast to the dynamical unfolding simulations used here, *Yamato et al.* [2011] used a numerical forward model. They found that the Hormuz Salt alone is not sufficient to explain the fold wavelength in the field. The modeled wavelength only agrees with the field observations when weak interlayer detachment horizons in addition to the Hormuz Salt allow for interfacial slip. There is also evidence for interfacial slip in the field. Besides the already mentioned Kolosh, Upper Shiranish, and Gercus Formations in the upper part of the cross section, also some of the Jurassic (Naokelekan, Sargelu, Chia Gara) and Cretaceous (Lower Balambo) formations contain thin-bedded shale layers, which may represent low-shear-strength surfaces separating otherwise mechanically strong lithologies and allow for interfacial slip between them.

[41] The weak interlayers introduce an effective anisotropy to the whole layer stack. Additionally to the weak interlayers between strong units, there may be thin marl or shale layers within a strong unit, which additionally act as local low-shear-strength layers. These layers cannot be explicitly modeled in the numerical simulations because they are too thin and too abundant to be resolved. However, they introduce an effective anisotropy to each individual unit, which can be approximated by a power law viscous rheology [*Fletcher*, 1974; *Kocher et al.*, 2006]. Therefore, the power law viscous rheology used in this study may represent dislocation creep as the deformation process as well as anisotropy due to unresolved weak layers or potentially due to foliation development. A power law exponent of  $n = 3$  represents well dislocation creep behavior in nature, while for approximating anisotropy the power law exponent may even be considerably higher. The same applies if the

power law viscous rheology is used to approximate an exponential flow law [*Schmalholz and Fletcher*, 2011] or plastic behavior. However, such complex rheologies represented by a large power law exponent have never been shown to give accurate results in dynamical unfolding simulations and are not considered here. For a power law exponent of  $n = 3$ , the simulations using power law viscous rheologies yield similar results as the simulations using a Newtonian rheology when no basement is present below the layer stack (Figures 8b, 8d–8f, and 9). However, including a basement increases the effect of the power law viscous rheology on the efficiency of dynamic unfolding (Figure 10). This can be understood because if the basement is close to the folded layers the strain rates are locally higher and more heterogeneous in the mechanically weak layer between basement and multilayer stack. Therefore, a power law viscous rheology can have more impact on the unfolding simulations for the case of a close basement.

[42] In general, kinematical restoration and unfolding models (e.g., Figure 7) underestimate the amount of horizontal shortening stored in a folded cross section because they do not include layer-parallel shortening prior to folding initiation [*Ghassemi et al.*, 2010; *Lechmann et al.*, 2010]. Dynamical unfolding does include this process. However, for natural fold profiles, dynamical unfolding is not capable of completely flatten the profile (MAD never reaches 100% in Figures 9 and 10). Residual fold amplitude always remains, no matter how much the profile is dynamically extended, a fact also observed by *Lechmann et al.* [2010]. Therefore, it is necessary to choose a critical residual amplitude (or MAD), at which the dynamical unfolding simulation is stopped. The dots in Figure 9 correspond to a critical MAD of 70%. This value was chosen arbitrarily and corresponds to a fold amplification of 233% in a forward simulation. Further investigations are necessary to better define the critical residual amplitude that should be used in dynamical unfolding simulations of natural fold profiles. Indeed, after the work of *Lechmann et al.* [2010], the presented study is only the second that applies dynamical unfolding to a natural fold profile and the method originally proposed by *Schmalholz* [2008] is still under development.

[43] Even though dynamical unfolding is not (yet) capable of fully flatten the folded profile, the simulation results are of great importance for planning future field investigations, as for example done by *Lechmann et al.* [2010]. The areas along the profile that are difficult to unfold are the same in all dynamical unfolding simulations. There may be two major reasons for these difficulties:

[44] 1. The constructed balanced cross section (Figure 5) contains unnatural geometries, such as sharp hinges.

[45] 2. These areas have a substantially different rheology or exhibit different physical processes in nature than in the numerical model.

[46] The first point can be due to sparse or inaccurate data, from which the cross section is constructed, or due to the construction method itself, which is used to extrapolate surface data upward and downward in the cross section. Areas that retain residual amplitudes during dynamical unfolding may correspond to areas in the constructed cross section, which are not well constrained by field data. Therefore, dynamical unfolding can help improve the balancing and construction of the cross section.

[47] Erosion is an important factor that can influence the dynamic unfolding simulations. Eroded anticlinal hinges cannot be properly mapped in a two-dimensional cross section, but can only be inferred from geological out-of-plane data. This may lead to inaccuracies in the balanced cross section. At the same time, erosion is currently not included in the numerical dynamical unfolding algorithm, even though it can influence the fold growth rate due to the removal of overburden. Although erosion is often modeled in forward simulations, it still needs to be implemented in a reverse time manner for the dynamic unfolding simulations. However, numerically inverting erosion and sedimentation in time may not be a trivial task.

[48] Relevant deformation processes in nature that are not included in the model are, for example, non-volume-conserving processes, such as solution-precipitation processes, compaction, or dewatering. Also, three-dimensional out-of-plane processes, such as fold-axis-parallel flow, are not included in the model, but may play an important role in nature. Finally, fracturing and faulting during folding may be another reason for the numerical simulation not being able to fully unfold the profile. Generally, the areas along the profile that are difficult to unfold correspond to thickened hinge zones in the original cross section (Figure 5), for example below the Safeen Anticline or between the Kamosk and the Pelewan Anticlines. Most probably, these hinge zones experienced space problems during the natural folding process. In a future field campaign, the deformation processes should be specifically investigated in the areas that were identified by the dynamical unfolding simulations as being difficult to unfold. Some of the above deformation processes, such as nonvolume-conserving processes or fracturing, still need to be tested on synthetic fold profiles before they can be used with confidence in dynamical unfolding simulations of real fold profiles.

## 6. Conclusions

[49] A cross section of the Zagros High Folded Zone in NE Iraq has been constructed from field and remote sensing data and used for kinematical and mechanical shortening estimation. For the mechanical estimate, dynamical unfolding simulations were performed using a numerical finite element model, taking into account different mechanical behaviors of the units. A comparison between classical length- and area-balanced cross-section reconstruction (11%–15% shortening) and dynamical unfolding simulations shows that very different shortening values can be calculated. In the kinematical estimates, the internal deformation of the units prior to folding, in particular layer-parallel shortening and thickening is ignored and shortening is generally underestimated. The disadvantage of dynamical unfolding is that it is generally not possible to completely flatten the profile. It is therefore not (yet) the goal of dynamical unfolding simulations to predict precise shortening values. However, areas along the profile that are difficult to flatten may help identify inaccurately constructed portions of the cross section, for example due to sparse or inaccurate field data, and dynamical unfolding simulations may be used as a quality control tool for cross-section constructions. Areas of residual amplitude in the dynamical unfolding simulations may also point to areas in the field where the

rheological behavior is fundamentally different than in the model. This can help define the focus of future field campaigns, where the rheological behaviors of these particular areas can be investigated in detail.

[50] Several different models for dynamical unfolding were tested. It can be concluded that the most critical factor for an efficient unfolding is the use of interfacial slip conditions. All models with interfacial slip result in realistic shortening values in the range of the highest kinematical estimates. For a critical MAD of 70% a shortening of less than 17% is found. Welded interfaces between the layers result in unrealistic high shortening values inconsistent with kinematical estimates. This allows concluding that interfacial slip along mechanically weak layers is an important deformation mechanism in the Zagros High Folded Zone in NE Iraq. Indeed, such thin layers are also described in the lithology of most of the modeled units. Other factors, such as power law viscous rheology or the presence of a basement, affect the resulting shortening estimates much less than interfacial slip.

[51] **Acknowledgments.** We thank the OMV Exploration and Production Company, Austria, for support and ideas as well as for organizing the field work; we especially thank Herwig Peresson, Gabor Tari, and Mohammad Fallah. Also many thanks to the employees of the OMV branch office in Erbil, Iraq, for providing support, logistics, and security during our stay in Erbil, including Dana Mawlood, Hunaar Majeed, Faris Habib Hanna, Ashty A. Karem, and many others. The three reviewers, Mary Ford, Boris Kaus, and Stefan Schmalholz, helped improve the original manuscript substantially and are acknowledged gratefully.

## References

- Alavi, M. (1994), Tectonics of the Zagros orogenic belt of Iran: New data and interpretations, *Tectonophysics*, 229(3–4), 211–238, doi:10.1016/0040-1951(94)90030-2.
- Alavi, M. (2004), Regional stratigraphy of the Zagros fold-thrust belt of Iran and its proforeland evolution, *Am. J. Sci.*, 304(1), 1–20, doi:10.2475/ajs.304.1.1.
- Bahroudi, A., and H. A. Koyi (2003), Effect of spatial distribution of Hormuz salt on deformation style in the Zagros fold and thrust belt: An analogue modelling approach, *J. Geol. Soc.*, 160, 719–733, doi:10.1144/0016-764902-135.
- Berberian, M. (1995), Master “blind” thrust faults hidden under the Zagros folds: Active tectonics and surface morphotectonics, *Tectonophysics*, 241(3–4), 193–224, doi:10.1016/0040-1951(94)00185-C.
- Bretis, B., N. Bartl, and B. Grasmann (2011), Lateral fold growth and linkage in the Zagros fold and thrust belt (Kurdistan, NE Iraq), *Basin Res.*, 23, 615–630, doi:10.1111/j.1365-2117.2011.00506.x.
- Burtscher, A., M. Frehner, and B. Grasmann (2012), Tectonic geomorphological investigations of antiforms using differential geometry (Permam Anticline, northern Iraq), *AAPG Bull.*, 96, 301–314, doi:10.1306/06141110204.
- Casciello, E., J. Vergés, E. Saura, G. Casini, N. Fernández, E. Blanc, S. Homke, and D. W. Hunt (2009), Fold patterns and multilayer rheology of the Lurestan Province, Zagros Simply Folded Belt (Iran), *J. Geol. Soc.*, 166, 947–959, doi:10.1144/0016-76492008-138.
- Cooper, M. (2007), Structural style and hydrocarbon prospectivity in fold and thrust belts: A global review, *J. Geol. Soc. Spec. Publ.*, 272, 447–472, doi:10.1144/GSL.SP.2007.272.01.23.
- de Vera, J., J. Gines, M. Oehlers, K. McClay, and J. Doski (2009), Structure of the Zagros fold and thrust belt in the Kurdistan region, northern Iraq, *Trab. Geol.*, 29, 213–217.
- Dieterich, J. H. (1969), Origin of cleavage in folded rocks, *Am. J. Sci.*, 267, 155–165, doi:10.2475/ajs.267.2.155.
- Fletcher, R. C. (1974), Wavelength selection in folding of a single layer with power-law rheology, *Am. J. Sci.*, 274, 1029–1043, doi:10.2475/ajs.274.9.1029.
- Frehner, M. (2011), The neutral line in buckle-folds, *J. Struct. Geol.*, 33(10), 1501–1508, doi:10.1016/j.jsg.2011.07.005.
- Frehner, M., and S. M. Schmalholz (2006), Numerical simulations of parasitic folding in multilayers, *J. Struct. Geol.*, 28(9), 1647–1657, doi:10.1016/j.jsg.2006.05.008.

- Ghassemi, M. R., S. M. Schmalholz, and A. R. Ghassemi (2010), Kinematics of constant arc length folding for different fold shapes, *J. Struct. Geol.*, *32*(6), 755–765, doi:10.1016/j.jsg.2010.05.002.
- Hessami, K., F. Nilforoushan, and C. J. Talbot (2006), Active deformation within the Zagros Mountains deduced from GPS measurements, *J. Geol. Soc.*, *163*, 143–148, doi:10.1144/0016-764905-031.
- Homke, S., J. Vergés, M. Garcés, H. Emami, and R. Karpuz (2004), Magnetostratigraphy of Miocene-Pliocene Zagros foreland deposits in the front of the Push-e Kush Arc (Lurestan Province, Iran), *Earth Planet. Sci. Lett.*, *225*(3–4), 397–410, doi:10.1016/j.epsl.2004.07.002.
- Hooper, R. J., I. R. Baron, S. Agah, and R. D. Hatcher (1995), The Cenomanian to recent development of the southern Tethyan margin in Iran, in *Geo '94: Middle East Petroleum Geosciences*, vol. 2, edited by M. I. Al-Husseini, pp. 505–516, Gulf PetroLink, Manama.
- Jassim, S. Z., and J. C. Goff (Eds.) (2006), *Geology of Iraq*, 352 pp., Dolin, Brno, Czech Republic.
- Kent, P. E. (1979), The emergent Hormuz salt plugs of southern Iran, *J. Pet. Geol.*, *2*(2), 117–144, doi:10.1111/j.1747-5457.1979.tb00698.x.
- Kocher, T., S. M. Schmalholz, and N. S. Mancktelow (2006), Impact of mechanical anisotropy and power-law rheology on single layer folding, *Tectonophysics*, *421*(1–2), 71–87, doi:10.1016/j.tecto.2006.04.014.
- Lan, L., and P. J. Hudleston (1991), Finite-element models of buckle folds in non-linear materials, *Tectonophysics*, *199*(1), 1–12, doi:10.1016/0040-1951(91)90115-9.
- Lechmann, S. M., S. M. Schmalholz, J.-P. Burg, and F. O. Marques (2010), Dynamic unfolding of multilayers: 2D numerical approach and application to turbidites in SW Portugal, *Tectonophysics*, *494*(1–2), 64–74, doi:10.1016/j.tecto.2010.08.009.
- Mancktelow, N. S. (1999), Finite-element modelling of single-layer folding in elasto-viscous materials: The effect of initial perturbation geometry, *J. Struct. Geol.*, *21*(2), 161–177, doi:10.1016/S0191-8141(98)00102-3.
- McQuarrie, N. (2004), Crustal scale geometry of the Zagros fold-thrust belt, Iran, *J. Struct. Geol.*, *26*(3), 519–535, doi:10.1016/j.jsg.2003.08.009.
- Molinaro, M., P. Leturmy, J.-C. Guezou, D. F. de Lamotte, and S. A. Eshraghi (2005), The structure and kinematics of the southeastern Zagros fold-thrust belt, Iran: From thin-skinned to thick-skinned tectonics, *Tectonics*, *24*, TC3007, doi:10.1029/2004TC001633.
- Mouthereau, F., J. Tensi, N. Bellahsen, O. Lacombe, T. De Boisgrollier, and S. Kargar (2007), Tertiary sequence of deformation in a thin-skinned/thick-skinned collision belt: The Zagros Folded Belt (Fars, Iran), *Tectonics*, *26*, TC5006, doi:10.1029/2007TC002098.
- Numan, N. M. S., R. A. Hammoudi, and J. Chorowicz (1998), Synsedimentary tectonics in the Eocene Pila Spi limestone formation in Iraq and its geodynamic implications, *J. Afr. Earth Sci.*, *27*(1), 141–148, doi:10.1016/S0899-5362(98)00052-9.
- Passchier, C. W., and R. A. J. Trouw (2005), *Microtectonics*, 2nd ed., 382 pp., Springer, Berlin.
- Reif, D., B. Grasemann, and R. Faber (2011), Quantitative structural analysis using remote sensing data: Kurdistan, northeast Iraq, *AAPG Bull.*, *95*, 941–956, doi:10.1306/11151010112.
- Schmalholz, S. M. (2008), 3D numerical modeling of forward folding and reverse unfolding of a viscous single-layer: Implications for the formation of folds and fold patterns, *Tectonophysics*, *446*(1–4), 31–41, doi:10.1016/j.tecto.2007.09.005.
- Schmalholz, S. M., and R. C. Fletcher (2011), The exponential flow law applied to necking and folding of a ductile layer, *Geophys. J. Int.*, *184*(1), 83–89, doi:10.1111/j.1365-246X.2010.04846.x.
- Schmalholz, S. M., Y. Y. Podladchikov, and D. W. Schmid (2001), A spectral/finite difference method for simulating large deformations of heterogeneous, viscoelastic materials, *Geophys. J. Int.*, *145*, 199–208, doi:10.1046/j.0956-540x.2000.01371.x.
- Schmalholz, S. M., Y. Y. Podladchikov, and J.-P. Burg (2002), Control of folding by gravity and matrix thickness: Implications for large-scale folding, *J. Geophys. Res.*, *107*(B1), 2005, doi:10.1029/2001JB000355.
- Schmid, D. W., Y. Y. Podladchikov, and F. O. Marques (2004), Folding of a finite length power law layer, *J. Geophys. Res.*, *109*, B03407, doi:10.1029/2003JB002421.
- Sepehr, M., J. Cosgrove, and M. Moieni (2006), The impact of cover rock rheology on the style of folding in the Zagros fold-thrust belt, *Tectonophysics*, *427*(1–4), 265–281, doi:10.1016/j.tecto.2006.05.021.
- Sherkati, S., J. Letouzey, and D. F. de Lamotte (2006), Central Zagros fold-thrust belt (Iran): New insights from seismic data, field observations, and sandbox modeling, *Tectonics*, *25*, TC4007, doi:10.1029/2004TC001766.
- Shimamoto, T., and I. Hara (1976), Geometry and strain distribution of single-layer folds, *Tectonophysics*, *30*(1–2), 1–34, doi:10.1016/0040-1951(76)90135-9.
- Sissakian, V. K., E. I. Ibrahim, and I. J. Al-Waily (1997), Geological map of Arbel and Mahabad Quadrangles, sheets Nj-38-14 and Nj-38-15, State Co. of Geol. Surv. and Min., Baghdad.
- Talbot, C. J., and M. Alavi (1996), The past of a future syntaxis across the Zagros, *Geol. Soc. Spec. Publ.*, *100*, 89–109, doi:10.1144/GSL.SP.1996.100.01.08.
- Tearpock, D. J., and R. E. Bischke (2003), *Applied Subsurface Geological Mapping With Structural Methods*, 2nd ed., 864 pp., Prentice Hall, Upper Saddle River, N. J.
- Vanoni, V. A. (2006), *Sedimentation Engineering: Theory, Measurements, Modeling, and Practice*, 2nd ed., 424 pp., Am. Soc. of Civ. Eng., Reston, Va.
- Vergés, J., E. Saura, E. Casciello, M. Fernández, A. Villaseñor, I. Jiménez-Munt, and D. García-Castellanos (2011), Crustal-scale cross-sections across the NW Zagros belt: Implications for the Arabian margin reconstruction, *Geol. Mag.*, *148*, 739–761, doi:10.1017/S0016756811000331.
- Yamato, P., B. J. P. Kaus, F. Mouthereau, and S. Castelltort (2011), Dynamic constraints on the crustal-scale rheology of the Zagros fold belt, Iran, *Geology*, *39*(9), 815–818, doi:10.1130/G32136.1.

M. Frehner, Geological Institute, ETH Zurich, NO E3, Sonneggstr. 5, CH-8092 Zurich, Switzerland. (marcel.frehner@erdw.ethz.ch, telephone: +41 44 632 5468, fax: +41 44 632 1030)

B. Grasemann and D. Reif, Department of Geodynamics and Sedimentology, University of Vienna, Althanstr. 14, A-1090 Vienna, Austria.